

Mineralogical variables that control the antibacterial effectiveness of a natural clay deposit

Keith D. Morrison · Jennifer C. Underwood ·
David W. Metge · Dennis D. Eberl ·
Lynda B. Williams

Received: 15 August 2013 / Accepted: 8 November 2013 / Published online: 21 November 2013
© Springer Science+Business Media Dordrecht 2013

Abstract As antibiotic-resistant bacterial strains emerge and pose increased global health risks, new antibacterial agents are needed as alternatives to conventional antimicrobials. Naturally occurring antibacterial clays have been identified which are effective in killing antibiotic-resistant bacteria. This study examines a hydrothermally formed antibacterial clay deposit near Crater Lake, OR (USA). Our hypothesis is that antibacterial clays buffer pH and Eh conditions to dissolve unstable mineral phases containing transition metals (primarily Fe^{2+}), while smectite interlayers serve as reservoirs for time release of bactericidal components. Model pathogens (*Escherichia coli* ATCC 25922 and *Staphylococcus epidermidis* ATCC 14990) were incubated with clays from different alteration zones of the hydrothermal deposit. In vitro antibacterial susceptibility testing showed that reduced mineral zones were bactericidal, while more oxidized zones had variable antibacterial effect. TEM

images showed no indication of cell lysis. Cytoplasmic condensation and cell wall accumulations of <100 nm particles were seen within both bacterial populations. Electron energy loss analysis indicates precipitation of intracellular Fe^{3+} -oxide nanoparticles (<10 nm) in *E. coli* after 24 h. Clay minerals and pyrite buffer aqueous solutions to pH 2.5–3.1, Eh > 630 mV and contain elevated level (mM) of soluble Fe (Fe^{2+} and Fe^{3+}) and Al^{3+} . Our interpretation is that rapid uptake of Fe^{2+} impairs bacterial metabolism by flooding the cell with excess Fe^{2+} and overwhelming iron storage proteins. As the intracellular Fe^{2+} oxidizes, it produces reactive oxygen species that damage biomolecules and precipitates Fe-oxides. The ability of antibacterial clays to buffer pH and Eh in chronic non-healing wounds to conditions of healthy skin appears key to their healing potential and viability as an alternative to conventional antibiotics.

Electronic supplementary material The online version of this article (doi:10.1007/s10653-013-9585-0) contains supplementary material, which is available to authorized users.

K. D. Morrison (✉) · L. B. Williams
School of Earth and Space Exploration, Arizona State
University, Tempe, AZ 85287, USA
e-mail: keith.morrison@asu.edu

J. C. Underwood · D. W. Metge · D. D. Eberl
U.S. Geological Survey, 3215 Marine St., Boulder,
CO 80303, USA

Keywords Antibacterial · Clays · Iron redox ·
Pyrite · Pathogens · Bacteria

Introduction

Emergence of antibiotic-resistant strains of bacteria presents a burgeoning global human health crisis. Traditional antibiotics, as organic molecules, inhibit DNA replication, protein and cell wall synthesis (Isakow et al. 2006), and many pathogens (e.g.,

Methicillin-resistant *Staphylococcus aureus*; MRSA) subsequently developed robust antibacterial resistance mechanisms. As a result, alternative therapies against bacterial infections have gained attention. Clay minerals, although used for medicinal purposes throughout millennia, have remained largely unstudied for their applications and reported medical benefits (Carretaro 2002; Ferrell 2008). Recent evidence reveals that certain clay mineral deposits that release soluble transition metals (when applied hydrated) have the ability to kill pathogenic bacteria growing in chronic skin infections (Brunet de Courrsou 2002; Williams et al. 2004, 2008). The use of metals as antimicrobial agents is growing (Lemire et al. 2013), and understanding the biochemical and geochemical mechanisms producing their antimicrobial effect is key to discovering new antibacterial mineral and metal compounds (Williams et al. 2011).

Previous studies of French green clays demonstrated highly effective antibacterial properties that were successfully used in treating *Mycobacterium ulcerans*, the causative pathogen of Buruli ulcers (Williams et al. 2004, 2008). Treatment with daily applications of hydrated clay poultices healed infection over the course of 3 months or more, by daily applications (Brunet de Courrsou 2002). These clays demonstrated a unique capacity to kill bacteria while promoting skin cell growth (Williams et al. 2004, 2008). Aqueous leachates of French green clays (deionized water shaken with minerals for 24 h) were also antibacterial. The leachate exhibited alkaline $\text{pH} \geq 9.8$ when prepared at a ratio of 100 mg clay/mL water then centrifuged to remove minerals. Unfortunately, the source of the French green clay minerals became depleted and subsequent testing of newer samples showed no bactericidal effect. Research on these French green clays spurred testing on various clay deposits and identification of several deposits that displayed antibacterial properties against a broad spectrum of human pathogens, including antibiotic-resistant strains (Cunningham et al. 2010; Williams and Haydel 2010; Williams et al. 2011). To date, the most effective antibacterial clays studied originate from hydrothermally altered regions near Crater Lake, OR, USA, marketed by Oregon Mineral Technologies (OMT).

In vitro antibacterial susceptibility testing of samples from the OMT deposit proved some to be bactericidal against a broad spectrum of bacteria,

including methicillin-resistant *S. aureus* (MRSA) and extended-spectrum beta-lactamase-resistant *E. coli* (ESBL) (Cunningham et al. 2010; sample CB07). Unlike the previously studied French green clays, all the antibacterial mineral suspensions examined from OMT have low pH (2.5–4.0). Williams et al. (2011) indicated iron uptake by *E. coli* cells upon reaction with OMT leachates. They first proposed that the chemical interaction between the clay leachates and the bacteria led to bactericide. Additionally, they proposed that the clay minerals buffer the pH and oxidation state to promote Fe^{2+} solubility thereby initiating a chemical attack via the Fenton reaction. However, the redox state of the iron was never directly measured. Bacterial iron assimilation occurred concurrent with the formation of large cytoplasmic voids and possible intracellular Fe^{3+} precipitation upon cell death (Williams et al. 2011).

Following this study, it was clear that more work was needed to evaluate how clays that differed in mineralogy, leachate chemistry, pH buffering capacity, and redox state affected the bactericide. Here we examine the detailed mineralogy of clays across the OMT deposit, the oxidation state of mineral suspensions, and the solution chemistry in relation to antibacterial effectiveness against model gram-positive and gram-negative bacteria. By measuring the cation exchange capacity of the clays, we further evaluated the role of the clay minerals in the antibacterial process. We find that the mixed-layered clay assemblage within the OMT antibacterial zones buffers aqueous solutions to low pH (2.5–4) and produces redox conditions that promote iron sulfide dissolution, generating aqueous metal species involved in the antibacterial process. The results show that mineralogical and geochemical variations across mineral alteration zones within OMT deposit produce variable bactericidal effects. These results will ultimately guide our understanding of important mineralogical constraints for identifying natural, mineral-based alternative antimicrobial agents.

Materials and methods

Geologic setting and mineral samples

Understanding the geological environments that produce antibacterial minerals is important for identifying

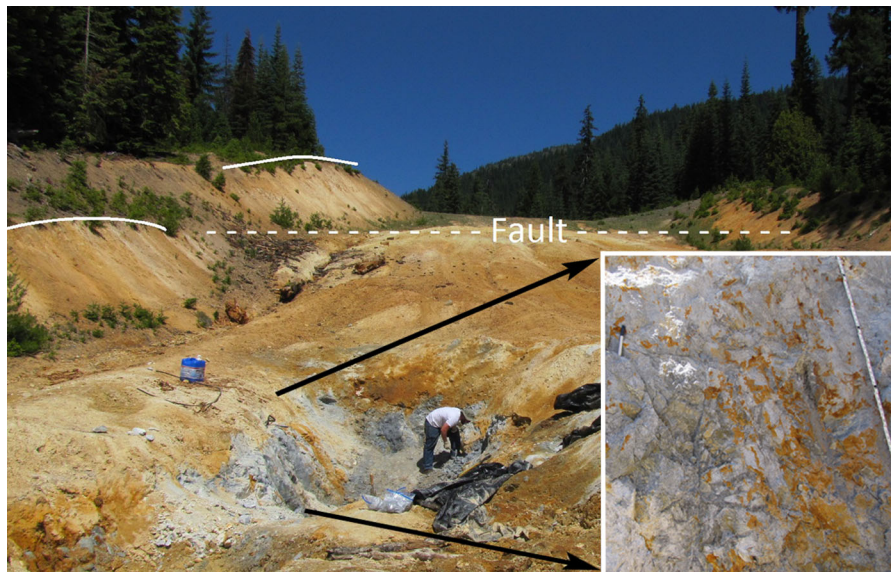


Fig. 1 Field area showing the open pit #10 of the OMT deposit. *Solid white lines* indicate the upper limit of the *Red* and *White* oxidized zones, which are covered by glacial till. *Black arrows* show a magnified image (16 cm marker for scale) of the

unoxidized *Blue zone* showing hydrothermally altered andesite. A series of NW–SE faults are present throughout the deposit along with an intricate stockwork of sulfide-rich *black veins*. (Color figure online)

other promising reserves and for evaluating the geochemical diversity within specific deposits that coincide with bactericidal activity. The Oregon Mineral Technologies (OMT) clay deposit, located in the Cascade Mountains (Douglas Co., OR, USA) near Crater Lake, is formed near volcanoes that have been active for tens to hundreds of thousands of years (Bacon 2008). This region is blanketed with volcanically derived pyroclastic and ash deposits. Ferrero (1992) estimated geologic ages of OMT clay between 20–30 million years, much older than the deposits of Mt. Mazama, which erupted only 7,700 years ago to form the Crater Lake caldera (Bacon 2008). However, regional volcanic eruptions over the last ~70,000 years produced silica-rich magmas and generated hydrothermal waters that may have contributed to the alteration of volcanoclastics in the OMT deposit.

Reconnaissance geologic mapping of the deposit (Ferrero 1992) showed that regionally, dacite and andesite altered to illite–smectite, pyrite and quartz along a major NW–SE trending fault. The alteration zones are exposed along a fault that defines the Foster Creek drainage. To the west, the OMT clay is covered by younger capping basalt, and to the east, the deposit is bound by a N–S trending fault zone aligned with the Rogue River drainage.

Samples for this study were taken from the main OMT open pit (#10). The primary host rock in this pit is a porphyritic andesite that has been hydrothermally altered to three main zones showing variations in oxidation conditions (redox) (Fig. 1). Oxidized red and white alteration zones found throughout the upper part of the deposit exposed in pit #10, range in thickness from 3 to 9 m. Unoxidized blue clays are pervasive stratigraphically beneath the oxidized zones and in some regions reach a thickness of 600 m (Ferrero 1992). Four representative samples were selected from the open pit for this study; two blue samples with variable antibacterial effectiveness were chosen, Blue 1, Blue 2, along with White and Red samples representing the major alteration units within this hydrothermal deposit.

Elemental sulfur, found in lenses stratigraphically below pit #10, exists in areas where sulfur mining occurred in the early 1900s. Highly sulfide-rich clay is black and associated with lenses of elemental sulfur but it was not exposed in the pit #10 sampled for this study. However, the mineral assemblage and presence of elemental sulfur are common in low-sulfidation epithermal alteration zones with low salinity, gas-rich (CO₂ and H₂S) reducing solutions ranging in temperature from 150 to 300 °C (Sillitoe and Hedenquist 2003).

Mineral analysis

X-ray diffraction

Oriented clay samples were prepared (<2.0 μm Na-exchanged) in air-dried and ethylene glycol saturated form to determine the mixed-layered illite–smectite content (Moore and Reynolds 1997). X-ray diffraction was performed using a Bruker D8-Focus diffractometer (ASU X-ray diffraction facility) with $\text{CuK}\alpha$ radiation. XRD patterns of mixed-layered clay minerals were calculated using NEWMOD© (Reynolds 1985).

Bulk clays, prepared for quantitative random powder XRD, followed procedures reported by Eberl (2007). Samples were crushed after drying at 60 °C overnight and passed through 250- μm sieves. Sieved samples were spiked with 20 % $\alpha\text{Al}_2\text{O}_3$ as an internal standard and micronized in ethanol using a McCrone Mill and then dried at 60 °C overnight. The micronized samples were then saturated with Vertrel® to ensure random orientation, sieved, and side-loaded into an XRD mount. All powdered samples were analyzed using a Siemens D-500 XRD with 1° divergence and receiving slits. Powdered samples were analyzed using $\text{CuK}\alpha$ radiation, scanning from 5° to 65° at 0.02° 2 θ steps with a 2 s per step count time. Quantitative mineralogy was calculated using the full pattern peak fitting program RockJock 11 (Eberl 2007). XRD patterns were fit from 19 to 64.5° 2 θ and all degrees of fit were <0.09 (supplementary data).

Elemental analysis

Prior application of antibacterial clay poultices exhibited bactericidal activity over 24 h time periods and were changed daily (Williams et al. 2004). Clay mineral leachates were also prepared to determine the role of soluble cations that may be playing a role in the antibacterial mechanism (Williams et al. 2011). Aqueous clay leachates were prepared by ultrasonically treating 50 or 100 mg/mL of bulk clay samples with deionized water (2 min), followed by shaking (24 h) to chemically equilibrate to the same degree represented by poultice applications, and finally centrifuged (15,000 rpm, 1 h) to separate minerals from the leachate. Elemental analyses of mineral leachates were performed using a Thermo X-series quadrupole ICP–MS (ASU, W.M. Keck Laboratory

for Environmental Biogeochemistry). Samples were acidified (nitric acid, 0.2 %) prior to analysis. Dilutions of 1:10 and 1:100 were analyzed along with undiluted samples and calibrated to multi-element reference standards. Certain elements (e.g., Si and S) are not ionized efficiently by ICP–MS or have interferences and therefore were not included in the analyses.

Quantitative assays of ferric, ferrous, and total iron

Mineral leachates were measured for Fe^{2+} , Fe^{3+} , and total iron immediately after centrifugation to remove minerals, using a method modified from Anastácio et al. (2008). The measurement of Fe^{2+} was performed under red photographic bulbs to prevent the photochemical reduction of the binuclear Fe^{3+} -phenanthroline complex to the Fe^{2+} -phenanthroline complex (Komadel and Stucki 1988). For the measurement of Fe^{2+} , a 50–500 μL aliquot of leachate was added to 1 mL of 2.5 wt% 1,10 phenanthroline (dissolved in 95 % ethanol). The solutions were then diluted with 1 wt% sodium citrate. Absorbance was measured with a spectrophotometer at 510 nm after 15 min for color development. Measurement of Fe^{3+} was achieved in the same manner using 200 μL of 10% hydroxylamine hydrochloride as a reducing reagent. Stock solutions of ferrous ammonium sulfate hexahydrate and ferric chloride (200 mg/L) were prepared and acidified using 3.6 N sulfuric acid to produce standard curves ranging from 1 to 8 mg Fe/L.

Eh, pH, and mineral titrations

All Eh, pH, and mineral titrations were measured using an Orion Dual Star pH, Eh meter (LE501 ORP and LE409 pH electrodes). The platinum Ag/AgCl (4 M KCl) Eh electrode was calibrated using Zobel solution resulting in a +220 mV offset with respect to a standard hydrogen electrode. All titrations were run in triplicate using 20 mL of a 100 mg/mL mineral suspension which was continually stirred and titrated with 0.1 N NaOH in 1 mL increments to a total of 50 mL using a burette. The pH meter was allowed to stabilize 1–5 min per addition between each addition of NaOH. A stability diagram for the Fe–S–O–H system was calculated using the CHNOSZ program (Dick 2008).

Cation exchange capacity

Cation exchange capacity (CEC) is a standard measure of the quantity of exchangeable cations that each clay sample can hold. CEC measurements were determined using cobaltichexamine chloride (Co(III)-hexamine) absorbance at 470 nm following methods of Aran et al. (2008) and Derkowski and Bristow (2012). Stock Co(III)-hexamine solutions (14.95, 7.48, 3.74, and 1.87 mM) were prepared to measure samples of varying CEC (Derkowski and Bristow 2012). Bulk mineral samples were placed in dialysis tubing and rinsed with 2 L of distilled–deionized (DDI) water 10 times to remove excess cations. Samples were dried (120 °C overnight) prior to measurement and 0.5–1 g portions were mixed with 25 mL of the stock solution. Samples were then sonicated for 2 min, shaken for 1 h and centrifuged (15,000 rpm, 10 min). Absorbance of supernatant solutions (470 nm) allowed measurement of molar concentration Co(III)-hexamine absorbed by clays. All CEC values are reported as milli-equivalents of charge per 100 g of sample (meq/100 g).

Bacterial analysis

Antibacterial susceptibility testing

Antibacterial susceptibility testing was performed on bulk mineral samples and aqueous mineral leachates. Samples were tested for antibacterial effectiveness against *E. coli* (ATCC 25922) and *S. epidermidis* (ATCC 14990). Bulk mineral samples were dried at 60 °C, crushed in a mortar and pestle, passed through a 250 µm sieve and autoclaved (121 °C, 15 psi, 30 min) to sterilize. The mineral samples (200 mg) were mixed with 400 µL of bacteria grown to exponential phase ($\sim 5 \times 10^7$ colony forming units per milliliter (CFU/mL)) in Luria–Bertani (LB) broth and incubated at 37 °C for 24 h. Triplicate serial dilutions (10-fold to 10^{-7}) were plated on LB agar plates.

Aqueous leachates were prepared from suspensions of 50 or 100 mg/mL of the bulk clay samples in deionized water, equilibrated 24 h (Williams et al. 2011). The aqueous leachates were separated from minerals by centrifugation as discussed above, mixed with bacteria in log-phase growth in LB (5×10^7 CFU/mL) in a 1:1 ratio by volume, incubated at 37 °C for

24 h, and then plated in LB agar and incubated for colony counting.

Transmission electron microscopy (TEM)

Transmission electron microscopy (TEM) imaging of bacteria, performed in a time series after mixing of cultures with mineral suspensions, provided visual evidence for physical changes to bacterial cellular membranes and internal structures as cells succumb to the clay-mediated bactericidal processes. Bulk clay suspensions (100 mg/mL) were equilibrated over 24 h of shaking and allowed to flocculate for 30 min forming a dilute mineral suspension. The reason for leaving some minerals in suspension was to look for attraction between the mineral and bacterial cells. Meanwhile, 10 mL of *E. coli* and *S. epidermidis* log-phase cells ($\sim 5 \times 10^7$ CFU/mL) was pelleted by centrifugation (5,000 rpm for 5 min) and re-suspended in isotonic sodium chloride (0.85 % NaCl) three times to remove LB broth. The pelleted cells were then exposed to 10 mL of the dilute mineral suspension in aqueous leachate, and 2 mL aliquots were sampled after 2, 8, and 24 h.

Aliquots of the reacted bacterial mineral suspensions were pelleted and chemically fixed using a 2.5 % glutaraldehyde solution buffered with PBS and stored at 4 °C overnight. Cells were then pelleted in 0.8 % low-melting point agarose to maintain the cells in dense aggregates. The cell pellets were subsequently fixed for 2 h using PBS-buffered 1 % osmium tetroxide, block-stained with aqueous 0.5 % uranyl acetate (overnight), and thoroughly washed in de-ionized water three times to remove all salts. The cells were slowly dehydrated using anhydrous acetone. Spurr's low viscosity epoxy resin (Spurr 1969) was used to infiltrate and embed the cells. The cells were then transferred into silicon molds and polymerized at 70 °C for 8 h. The resin blocks were sectioned using a Leica Ultracut-R ultramicrotome and a diamond knife. Ultrathin sections were cut to 60–70 nm thickness and mounted on Formvar-coated TEM grids (Lawrence et al. 2003; Liss et al. 1996). A final staining with 2 % uranyl acetate and Sato's lead citrate (Hanaichi et al. 1986) was performed prior to imaging. TEM images were collected using a Philips CM12 transmission electron microscope operated at 80 kV (Arizona State University, Bio-imaging Facility).

Scanning transmission electron microscopy (STEM)

Bacteria–mineral suspensions were also imaged using STEM and electron energy loss spectroscopy (EELS) to determine the elemental composition of intracellular precipitates. Aliquots of the bacterial–mineral suspensions were pelleted after reacting for 24 h at 37 °C. Samples were then fixed using a BalTec HPM010 high-pressure freezer and freeze substituted using 2 % osmium tetroxide, embedded in Spurr's resin, sectioned (60 nm) and mounted on Cu TEM grids (Spurr 1969; Walther and Ziegler 2002). Osmium tetroxide was the only stain used during fixation to avoid additional electron scatter from lead citrate and uranyl acetate during EELS analysis. STEM images and EELS were collected using a JEOL 2010F TEM/STEM at 200 kV and a resolution of 0.5 eV to image O–K edge and Fe–L_{2,3} and 0.3 eV to determine the redox state of the Fe–L_{2,3} edges (Arizona State University, LeRoy Eyring Center for Solid State Science).

Results

Quantitative X-ray diffraction

The mineralogy of the OMT deposit (Table 1; Fig. 2) is dominated by mixed-layered illite–smectite clay minerals (43–53 %) and quartz (36–49 %). NEW-MOD modeling (Reynolds 1985) of the <2.0 μm oriented glycolated XRD patterns indicates that all samples contain a complex mixture of various illite–smectite interlayering (Meunier 2005). Mixtures of 95 % illite–smectite (IS) ($R > 3$) and 70 % IS ($R > 1$) provided the best fits using RockJock 11 and NEW-MOD (Supplementary data).

Samples from the upper oxidized zones (Red and White) located stratigraphically above the Blue zone contained no measurable pyrite. The main iron-bearing mineral phase within Red zones is goethite. In addition to the I–S, minor kaolinite and chlorite are present in the Red zone. The White zone sample contained 6.3 % smectite in addition to the I–S and trace kaolinite. The Blue samples from the unoxidized zone each contain several weight percent pyrite, a potential source for Fe²⁺. Secondary minerals gypsum, jarosite, and goethite are present as well and these are characteristic of acid mine drainage environments

Table 1 Mineralogy of OMT mineral deposit measured by quantitative X-ray diffraction using RockJock 11

Mineral	Blue 1 Wt%	Blue 2 Wt%	White Wt%	Red Wt%
Quartz	41.1	44.6	48.5	36.3
Pyrite	3.0	4.5	n.d.	n.d.
Gypsum	1.2	0.8	2.7	n.d.
Jarosite	n.d.	1.5	n.d.	n.d.
Goethite	n.d.	n.d.	n.d.	3.4
Albite	n.d.	0.4	1.7	4.4
Andesine	1.2	n.d.	0.6	0.2
Anorthite	1.2	0.6	0.6	n.d.
Total (non-clays)	47.7	52.4	54.1	44.3
Kaolinite	n.d.	0.4	0.2	4.7
Chlorite (Fe-rich)	n.d.	n.d.	n.d.	3.5
Smectite (Ca)	n.d.	n.d.	6.3	n.d.
Illite–smectite	n.d.	n.d.	n.d.	n.d.
($R > 1$, 70–80 % I)	22.9	45.7	21.6	40.9
($R > 3$, 95 % I)	26.9	n.d.	15.0	3.7
Total (clays)	49.8	43.4	43.1	52.8

Minerals not detected are listed as (n.d.)

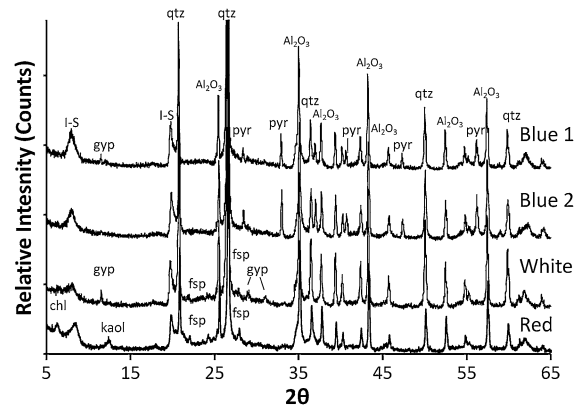


Fig. 2 Random powder XRD patterns spiked with internal standard (Al_2O_3), showing the presence of quartz (*qtz*), feldspar (*fsp*), gypsum (*gyp*), pyrite (*pyr*), mixed-layered illite–smectite (*IS*), kaolinite (*kaol*), and chlorite (*chl*)

(Murad and Rojik 2004, 2005). Plagioclase feldspars (albite, andesine, anorthite) from the host andesite are identified in all of the samples.

Antibacterial susceptibility testing

Results from the in vitro antibacterial susceptibility testing (Fig. 3a, b) show that bulk mineral suspensions

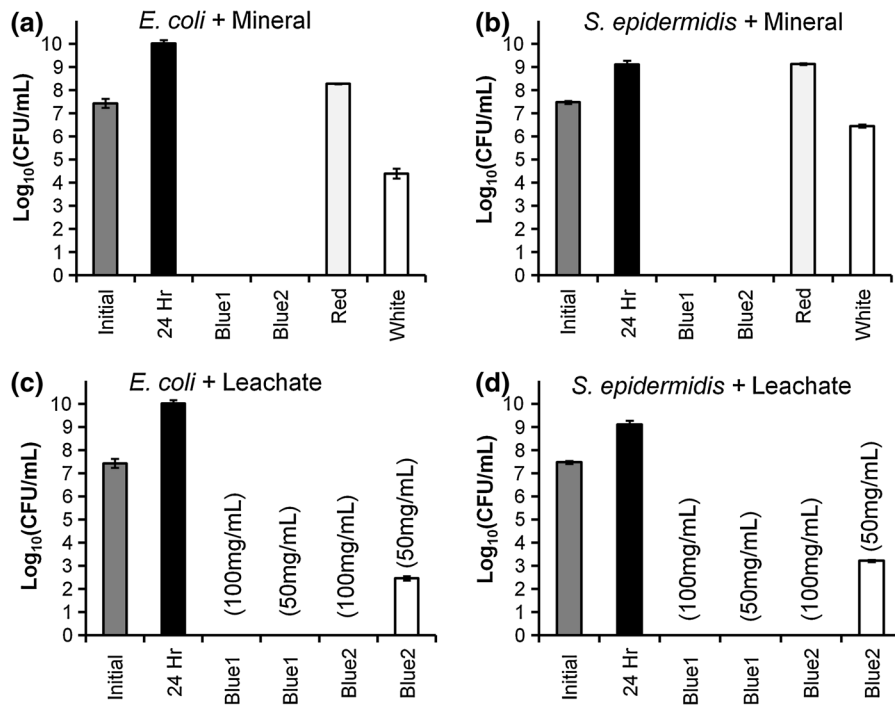


Fig. 3 Antibacterial susceptibility testing of OMT mineral samples (500 mg/mL) (a, b) and leachates as indicated (c, d) reacted with *E. coli* and *S. epidermidis* for 24 h. Bacterial

control colony forming units (CFU/mL) were measured at the initial time of reaction with the minerals or leachates and again after 24 h

(500 mg/mL) of the OMT Blue samples (Blue 1 and 2) were completely bactericidal against *E. coli* and *S. epidermidis*. The White sample reduced the population of *E. coli* and *S. epidermidis* by 56 and 29 %, respectively, while the Red sample did not affect the growth compared to the 24-h control, grown without clays.

Results from experiments with aqueous leachates are shown for comparison (Fig. 3c, d). Different concentrations of the Blue clays were tested to discern differences in their antibacterial potency. The 100 and 50 mg/mL leachates from the Blue 1 sample were completely bactericidal against both bacterial species. The 100 mg/mL leachate from the Blue 2 sample was also bactericidal, but the 50 mg/mL leachate from Blue 2 only inhibited bacterial growth by 75 and 65 % for *E. coli* and *S. epidermidis*, respectively. Leachates from the White sample (100 mg/mL) were not antibacterial (results not shown).

Leachate chemistry and elemental analysis

Results from the ICP–MS elemental analysis are given in Table 2, along with published minimum

inhibitory concentrations (MIC) and minimum bactericidal concentrations (MBC) for metals tested against *E. coli* (Nies 1999; Harrison et al. 2005). MICs and MBCs are used to measure the antibacterial potency of a compound. The MIC is defined as the lowest concentration of an antibacterial compound that prevents visible bacterial growth (optical density at 600 nm) in nutrient broth. The MBC is defined as the minimum amount of an antibacterial compound which causes a 99.9 % reduction in bacterial growth measured by plating and CFU counting (Wilson et al. 1990; Harrison et al. 2005). The Blue 1 and Blue 2 leachates each contained mM levels of Fe, Al, and Ca (Table 2). No MIC or MBC is reported for Fe and Ca because these elements are generally bacterial nutrients (Nies 1999; Harrison et al. 2005). The Blue 1 leachate was above the 2 mM MIC for Al at both mineral and fluid ratios tested (50 and 100 mg/mL) while the Blue 2 leachate only surpassed the MIC in the 100 mg/mL leachate. Concentrations of other potentially toxic elements (Ag, As, Cd, Co, Cr, Cu, Ni, Mn, Pb, V, and Zn) are well below published MIC and MBC values.

Table 2 ICP–MS elemental analysis and pH of mineral leachates from clay/fluid concentrations indicated (mg/mL)

Element	Blue 1 100 mg/mL	Blue 1 50 mg/mL	Blue 2 100 mg/mL	Blue 2 50 mg/mL	White 100 mg/mL	Red 100 mg/mL	Ion Species	<i>E. coli</i>	
								^a MIC	^b MBC
Na	67.07	36.09	29.78	16.6	39.1	43.4			
Mg	1,128.28	568.84	410.88	213.7	274.3	13.8			
Al	5,047.86	2,451.87	2,337.34	1,097.2	456.3	54.4	(Al ³⁺)	2,000	19,000
P	277.92	79.44	110.47	22.2	1.7	1.20			
K	34.69	25.46	15.18	11.5	44.2	11.8			
Ca	6,617.68	3,419.08	2,015.89	1,054.5	11,176.1	35.8			
Ti	0.89	0.45	0.27	0.12	0.28	2.81E–02			
V	2.07	1.1	2.18	0.79	4.73E–03	2.67E–02	(V ³⁺)	5,000	
Cr	1.22	0.68	0.59	0.25	0.12	1.15E–02	(Cr ³⁺)	5,000	
Mn	45.6	22.6	7.1	3.51	11.8	0.19	(Mn ²⁺)	20,000	198,000
Fe	18,030.4	9,752.8	7,052.7	2,954.3	728.7	11.9		–	–
Co	11.4	5.8	3.73	1.92	0.40	2.75E–03	(Co ²⁺)	1,000	
Ni	11.8	6.1	5.6	2.85	0.38	8.67E–03	(Ni ²⁺)	1,000	17,000
Cu	11.7	6.0	4.1	2.21	1.9	4.27E–02	(Cu ²⁺)	1,000	16,000
Zn	4.3	2.2	5.7	2.96	2.8	9.57E–02	(Zn ²⁺)	1,000	31,000
As	2.2	0.74	0.46	8.52E–02	BDL	BDL	(AsO ₂ [–])		75,000
Se	0.22	0.12	BDL	6.79E–02	4.38E–02	BDL	(SeO ₃ ^{2–})		13,000
Rb	0.18	0.12	4.21E–02	2.80E–02	6.36E–02	5.85E–03			
Sr	26.8	14.8	2.5	1.28	7.9	0.15			
Zr	5.89E–04	2.06E–04	1.90E–04	0.31	2.61E–04	9.68E–04			
Mo	0.22	0.11	1.01E–01	0.05	2.60E–02	2.49E–03			
Ag	2.44E–04	1.29E–04	6.34E–05	BDL	2.04E–04	7.79E–05	(Ag ⁺)	20	60
Cd	6.84E–03	4.30E–03	4.19E–03	2.12E–03	1.61E–03	BDL	(Cd ²⁺)	500	2,300
Cs	6.68E–02	4.67E–02	2.41E–02	1.60E–02	5.76E–03	2.34E–03			
Ba	4.86E–02	8.29E–02	0.17	2.03E–01	1.07E–01	1.34E–02			
Hf	7.38E–04	3.80E–04	5.21E–04	2.66E–04	2.25E–04	4.77E–05			
W	6.88E–03	9.19E–04	1.69E–03	BDL	6.02E–04	BDL			
Au	BDL	BDL	BDL	BDL	BDL	BDL	(Au ³⁺)	20	
Hg	BDL	BDL	BDL	BDL	BDL	BDL	(Hg ²⁺)	10	40
Pb	4.01E–03	2.60E–03	1.07E–02	3.54E–02	3.37E–04	3.04E–04	(Pb ²⁺)	5,000	
U	2.78E–03	1.36E–03	3.61E–03	1.66E–03	1.84E–03	2.50E–05	(UO ₂ ^{2–})		
pH	2.5	2.9	2.9	3.1	3.1	6.5			
Eh (mV)	682.2	661.7	705.8	702.5	630.4	448.7			

Elemental concentrations are reported in micro-molarity (μM). All bacteria growing in LB were reacted with leachates in a 1:1 ratio. All relative standard deviation values ≤5 % and samples <10 nM are listed as below detection limit (BDL).

^a Minimum inhibitory concentration (MIC) of metals (24 h) for *E. coli* determined using Tris-buffered mineral salts medium (pH 7), with 2 g/L Na-gluconate and 1 g/L yeast extract (29, 36, 56)

^b Minimum bactericidal concentration (MBC) of metals (24 h) for *E. coli* determined using Luria–Bertani medium enriched in vitamin B1 (30)

In studies of human pathogens, the toxicity of iron is traditionally not considered due to its low solubility (10^{–18} M) at circumneutral pH. However, the natural mineral–water suspensions studied here have distinctly

different solution pH and Eh, which influence the solubility of metals. The pH and Eh measurements for the OMT Blue and White samples (Table 2) ranged from 2.5 to 3.1 and 630.4 to 705.8 mV, respectively.

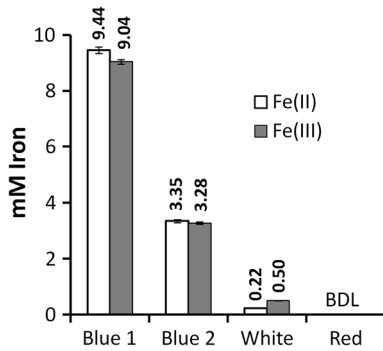


Fig. 4 Ferrous and ferric iron levels of 100 mg/mL mineral leachates. Fe²⁺ and Fe³⁺ concentrations (mM) are listed for each sample. The Red sample was below the detection limit (BDL) of 1 μM Fe

The Red sample showed the highest pH (6.5) and lowest Eh (448.7 mV).

The results from the ferrous and ferric iron assay (Fig. 4) show the presence of both Fe²⁺ and Fe³⁺ in 100 mg/mL leachates of the Blue 1, 2 and White samples, with no measureable Fe²⁺ in the Red (most oxidized) sample near neutral pH, given a detection limit of 1 μM. The Blue 1 and 2 samples contain ferrous iron in approximately equal proportion to ferric iron. The Blue 1 leachate contained the greatest amounts of iron with 9.04 mM Fe³⁺ and 9.44 mM Fe²⁺ while the Blue 2 leachate had 3.28 mM Fe³⁺ and 3.35 mM Fe²⁺. The White leachate contained 0.50 mM Fe³⁺ and 0.22 mM Fe²⁺.

Electron microscopy

Figure 5 compiles the TEM images of *E. coli* and *S. epidermidis* cells in their initial healthy condition and in time series (2, 8 and 24 h) after incubation with the bactericidal Blue 1 mineral suspension (100 mg/mL). The presence of intact bacterial cell membranes indicates that cell lysis is not the main antibacterial mechanism; however, membrane permeability may still be compromised. Both bacterial species accumulated extracellular mineral particles (20–100 nm diameter), which did not appear to disrupt the cell walls; however, textural differences are observed in the response of the gram-negative and gram-positive cells over time. *E. coli* cells exhibited greater changes in their cell morphology than *S. epidermidis*. Cytoplasmic condensation occurred in *E. coli* after 8 and 24 h (Fig. 5c, d) resulting in electron transparent voids

and small (5–10 nm) particles throughout the cytoplasm similar to those reported by Williams et al. (9). The *S. epidermidis* cells develop a less electron dense region surrounding the cell envelope after 2 h of reaction (Fig. 5f). After 8 and 24 h (Fig. 5g, h), the *S. epidermidis* cells regain contrast in their cell walls and display adhesion of (<5 nm) mineral particles. After 8 and 24 h, both *E. coli* and *S. epidermidis* cells show an electron dense zone surrounding their cell walls. The *S. epidermidis* cells also show hair like wisps on the exterior cell walls (Fig. 5f–h).

The composition of the intracellular particles was measured using STEM-EELS. Figure 6 shows STEM dark field images of *E. coli* cells reacted with a Blue 1 mineral suspension (100 mg/mL) and fixed using high-pressure freezing. EELS measurements of intracellular and extracellular particles reveal the presence of O–K edge and Fe–L_{2,3} edge spectra. Accumulations of mineral particles outside the cell appear to be 20–100 nm Fe-oxide particles (Fig. 6a). The intracellular nanoparticles are smaller in size (<10 nm) and are also Fe-oxides. A second EEL spectrum of the intracellular particles was measured at a resolution of 0.3 eV revealing only Fe³⁺ particles at 709.5 eV (Fig. 6d). Other elements that may play a role in antibacterial processes (e.g., Al, Ag, Cu, Zn) were not detected intracellularly.

Cation exchange capacity

Cation exchange capacity (CEC) measurements of the bulk minerals and <2 μm clay fractions are shown in Fig. 7. The bulk mineral samples exhibited similar CEC with values ranging from 14.5 to 19.1 meq/100 g. Measurements of the clay-sized fraction showed slightly higher CEC for all clays due to an increased concentration of phyllosilicates in this size fraction. The highest CEC (33.4 meq/100 g) is observed in the <2 μm clay size fraction of the White sample that contains 6.3 wt% smectite (Table 1).

Mineral titrations

The pH buffering capacity of the mineral suspensions was determined using NaOH titration of 100 mg/mL bulk clay suspensions. Titration curves for each sample are shown in Fig. 8. The Blue 1 sample has the highest buffering capacity because it takes more base addition to change the pH. Solutions from the

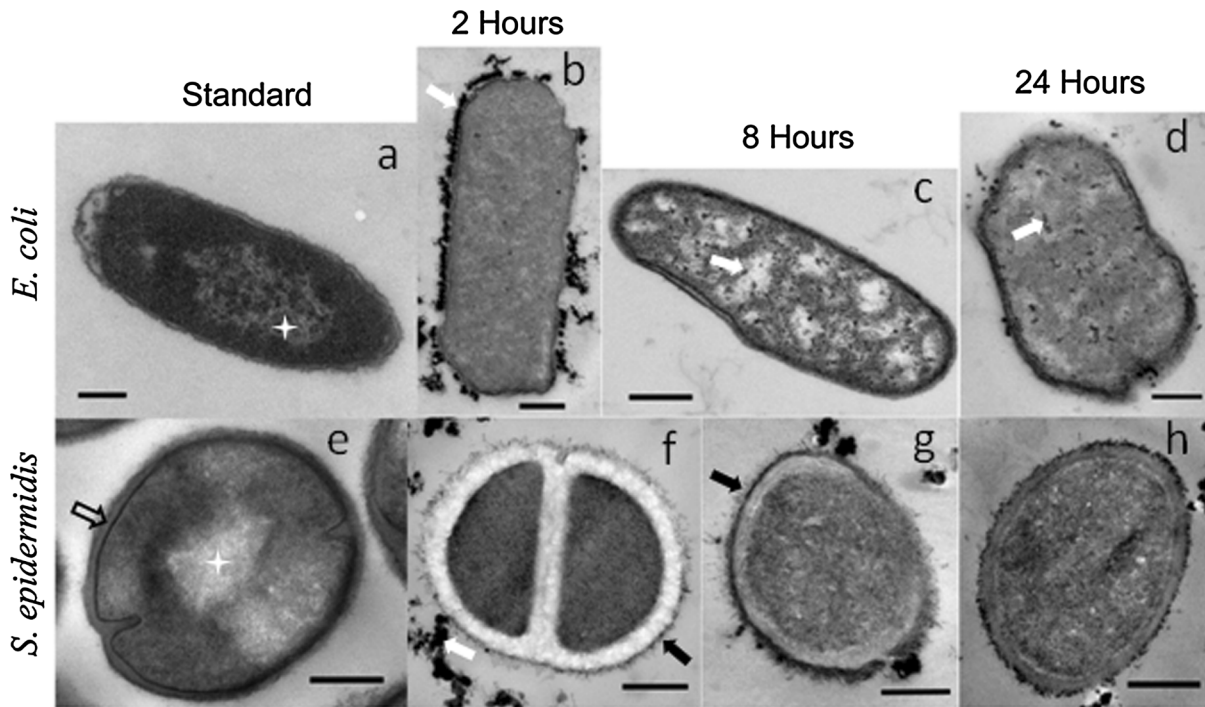


Fig. 5 TEM images of gram-negative *E. coli* and gram-positive *S. epidermidis* reacted with 100 mg/mL OMT Blue 1 mineral suspensions (Scale bars 250 nm). White stars indicate bacterial nucleoid (a, e). Hollow black arrow shows peptidoglycan layer

(e). Solid white arrows indicate mineral particles and electron dense particles within the cytoplasm (c, d, f). Solid black arrows point to thread like appendages coated with electron dense particles (f, g)

Blue samples may be buffered by the hydrolysis of Fe^{3+} (pH < 3.8), Al^{3+} (pH 3.5–4.5), and Fe^{2+} (pH 5.5–6.5) cations (Dold 2005; Totsche et al. 2006). The less antibacterial Blue 2 and White samples had lower buffering capacity compared to Blue 1. The Red sample showed no buffering capacity. Zones for Fe^{2+} , Fe^{3+} , and Al^{3+} buffering capacity are shown in shaded regions (Fig. 8) (Dold 2005; Totsche et al. 2006).

Discussion

Antibacterial effectiveness

In this study, the mineralogy, solution chemistry, and antibacterial activities were compared between samples representing different mineral alteration zones within the OMT clay deposits. We proposed that antibacterial activities relate to the mineralogy and redox state of the hydrated clays when applied to pathogenic bacteria. To test this, we measured the antibacterial effectiveness as a function of mineralogical changes and chemical variables across the deposit.

The level of antibacterial activity correlates with mineralogical variables controlling pH and redox conditions which in turn influence element solubility and exchange between minerals and bacteria.

Clays in natural geologic environments represent diverse mixtures of minerals <2 μm in diameter (Moore and Reynolds 1997). When antibacterial clays are hydrated with DDI water, a series of spontaneous reactions occur as a new chemical equilibrium is approached (Williams et al. 2008). These conditions are different from those established within the natural geologic setting. Results from our antibacterial susceptibility testing and quantitative mineralogy indicate that samples containing pyrite (Blue 1 and 2) are the most antibacterial (Table 1; Fig. 3). However, the White sample, which does not contain pyrite or any other detectable sulfides, still prevented bacterial growth (Fig. 3). The Red sample was not antibacterial and contained no measurable pyrite, but did contain the Fe-oxide goethite (3.4 %), a common pyrite oxidation product (Hutchinson and Ellison 1992).

The consistently high abundance of Fe associated with the most antibacterial OMT samples points to its

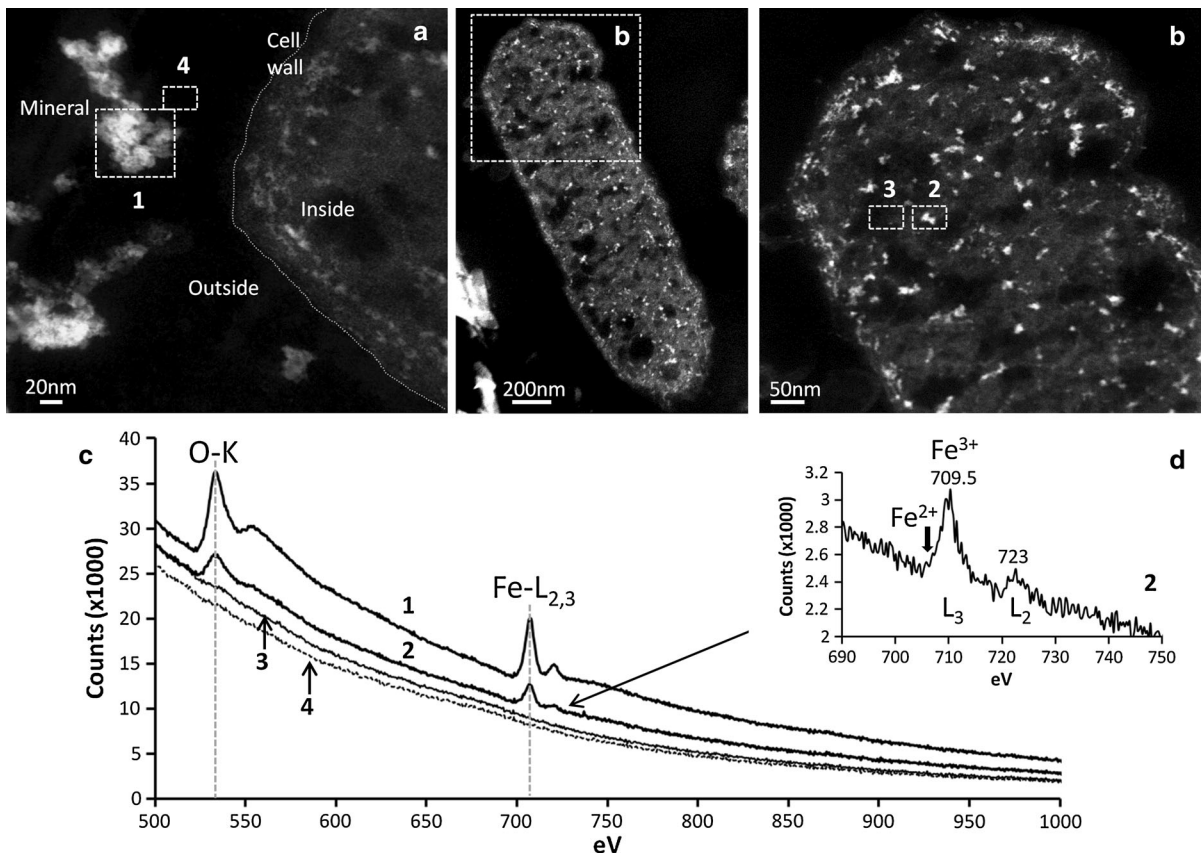


Fig. 6 STEM dark field images (contrast reversed from TEM images, Fig. 5) and electron energy loss (EELS) in eV of *E. coli* reacted with a 100 mg/mL Blue 1 mineral suspension for 24 h. **a** Mineral particles outside the cell range in size from 20 to 100 nm; **b** intracellular particles (<10 nm) are shown in two separate images with 200 and 50 nm scale bars; **c** EELS spectra

of the oxygen K edge (533 eV) and iron L-2/3 edge (709.5 eV) with 0.5 eV resolution. Both the extracellular and intracellular mineral particles are composed primarily of iron and oxygen. The iron L-2/3 edge of the intracellular particles (0.3 eV resolution) reveals the presence of Fe³⁺ at 709.5 eV; Fe²⁺ at 707.5 eV shown in inset **d** was not measurable

involvement in the bactericidal process. While the most potent antibacterial sample (Blue 1) contains the highest amount of soluble Fe²⁺ (9.5 mM) in its leachate, the Blue 2 contains only 3.45 mM of soluble Fe²⁺, even though the clay contains 1.5 wt% more pyrite than Blue 1. These data suggest a different solubility of Fe²⁺ between these samples from the same Blue zone. The difference can be due to mineralogy or redox conditions. There are two iron sulfide morphologies; discrete pyrite crystals (20–40 μm) and amorphous nanometric iron sulfides spherules (~20 nm) (Williams et al. 2011). If Blue 2 contains a greater amount of crystalline pyrite, it would be less soluble than the amorphous iron sulfide. Alternatively, the lower Fe²⁺ content of Blue 2 could result from its higher oxidation state (Table 2) that

may favor the precipitation of iron-bearing mineral phases, thus lowering the total Fe in solution. The precipitation of secondary minerals such as jarosite, uniquely present in the Blue 2 sample (1.5 wt%), can lower pyrite oxidation rates by coating the pyrite (Hutchinson and Ellison 1992; Murad and Rojik 2005). The oxidation of pyrite results in a cascade of redox reactions (discussed below) that lower pH and release both ferrous and ferric iron into solution, impacting the metabolism of environmental microbes, in a different way than microbes that evolved to inhabit humans (Garrels and Thompson 1960; Nies 2003).

It is important to note that, while the OMT Blue clays are antibacterial against a broad spectrum of human pathogens (Cunningham et al. 2010), there are

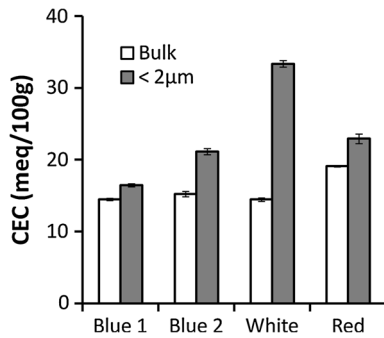


Fig. 7 Cation exchange capacity (CEC) measurements for bulk mineral s and $<2\ \mu\text{m}$ Na-exchanged clay fractions. All results are expressed as milli-equivalents of charge per 100 g of mineral (meq/100 g)

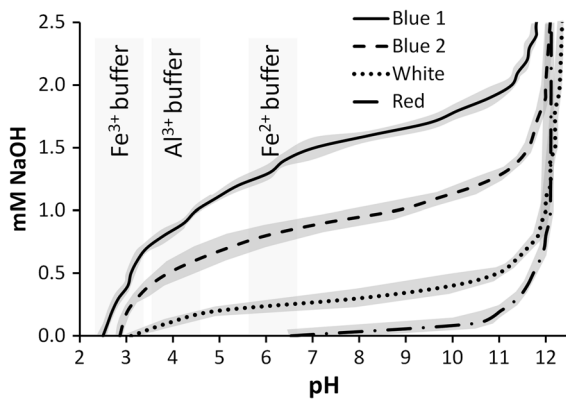


Fig. 8 Titrations of 100 mg/mL mineral suspensions with NaOH (0.1 N). Gray regions outlining the titration curves represent the standard deviation of each sample run in triplicate. Zones for Fe^{2+} , Fe^{3+} , and Al^{3+} buffering capacity shown in shaded regions (Dold 2005; Totsche et al. 2006)

environmental microbes that have evolved to survive in the natural environment and are metabolically active in the clay. Isolation of environmental microbes from an OMT Blue sample showed that the genus *Burkholderia* comprises the majority of bacteria living in the low pH, metal-rich conditions (pers. comm. Weimin Gao, ASU Bidesign Institute). The genus *Burkholderia* is metabolically diverse and contains 58 species (Bhowal and Chakraborty 2011). Isolates of *Burkholderia* have been found in acidic soils (pH 2.9), iron ores, and acid mine drainage (pH 1.5–3) (Valverde et al. 2006; Church et al. 2007; Bhowal and Chakraborty 2011). *Burkholderia* growing in acid mine drainage settings are chemolithoautotrophic and oxidize thiosulfate to sulfate (Bhowal and Chakraborty 2011). Acidophilic bacteria exhibit more robust

metal efflux systems and different membrane lipid compositions compared to human pathogenic bacteria, which evolved to survive in iron-limited environments (Ratledge and Dover 2000; Nies 2003).

Given that human pathogens evolved to thrive under circumneutral pH conditions with limited Fe availability, one might suspect that acidic, metal-rich conditions imposed by topical application of OMT Blue clays would compromise cell integrity. However, TEM images (Fig. 5) do not support cell lysis as a dominant antibacterial mechanism for OMT clays. While many antibacterial agents damage peptidoglycan peptide linkages and induce lysis (Silhavy 2010), the OMT bacterial cells treated with OMT Blue clays maintain their rigidity and structure. Accumulation of mineral particles around bacterial cells did not appear to penetrate cell walls or disrupt the peptidoglycan layers (Fig. 5), but both *E. coli* and *S. epidermidis* cells showed cytoplasmic condensation, and intracellular accumulation of $<10\ \text{nm}$ electron dense particles. The *S. epidermidis* appeared more resistant to cytoplasmic condensation and had fewer cytoplasmic particles. An electron transparent region surrounding the *S. epidermidis* cells appeared after 2 h (Fig. 5f), which could result from secretion of a protective layer of polysaccharides (*N*-acetyl-glucosamine) that has been reported to allow *S. epidermidis* cells to adhere to surfaces and resist environmental stress (Götz 2002). These polysaccharides appear transparent because none of the chemical stains used in TEM preparation (osmium tetroxide, lead citrate and uranyl acetate) bind to these exo-polysaccharides to provide contrast. This layer is not observed at longer incubation times, suggesting that the defense mechanism failed and infiltration of toxins began.

Williams et al. (2011) suggested that a flood of Fe^{2+} through the cell wall might have generated intracellular reactive oxygen species (ROS) responsible for the cytoplasmic condensation, resulting in precipitated Fe^{3+} nano-particles; however, the composition of the electron dense particles was not confirmed. Here, results from the STEM–EELS confirm that these particles are composed of iron and oxygen (Fig. 6). Rapid Fe^{2+} uptake and oxidation to Fe^{3+} is likely responsible for the intracellular Fe-oxide nanoparticles due to the fact that Fe^{2+} is taken into the cell with rapid unspecific chemiosmotic uptake mechanisms, while Fe^{3+} requires siderophore-based transport (Nies 2003). If cytoplasmic Fe^{2+} levels exceed cellular

demand oxidation to Fe^{3+} and storage in ferritin occurs in order to keep free Fe^{2+} at low concentrations (Smith 2004). The influx of Fe^{2+} into the cell could overwhelm iron storage proteins potentially leading to toxic levels of free Fe^{2+} , while oxidation leads to precipitation of iron oxide nanoparticles which cannot be removed by efflux. As these intracellular iron nanoparticles are precipitating, ROS may also be generated leading to more oxidizing conditions inside the cell. The STEM–EELS and EDS (data not shown) analysis did not reveal the presence of intracellular Al^{3+} , nor have bulk analytical methods indicated that Al^{3+} is entering the cell (Williams et al. 2011). Trivalent Al does not normally diffuse through cell walls (Nies 1999) and if it is chelated and makes it through the membrane, the cells quickly expel it (Williams 1999). At low pH (<4.5), AlOH^{2+} may be stable on the cell wall, competing with Ca^{2+} binding sites, and can lead to precipitation of aluminosilicates (Urrutia and Beveridge 1995).

Cation exchange

In low pH (<4) acid mine drainage, smectite has been shown to fully dissolve (Galan et al. 1999). However, kaolinite and illite show little change in their crystal chemistry when exposed to these acid conditions (Galan et al. 1999; Shaw and Hendry 2009). The mixed-layered illite–smectite found in the OMT deposit may be more resistant to acid dissolution because of its high illite content (>70 %; Table 1), while the smectite is protected by the surrounding illite, allowing the expandable interlayer to act as a reservoir for exchangeable cations. Therefore, if dissolution of pyrite supplies abundant Fe^{2+} , it may be adsorbed in the expandable smectite interlayers. The pH in the interlayer of expandable clay minerals can be several log units lower than that of the bulk (external) solution (Yariv 1992; Yariv and Cross 2002). The lower acidity of the interlayer may slow the oxidation rate of reduced iron (Singer and Stumm 1970).

Exchangeable Fe^{2+} in illite–smectite from a natural deposit would be released from the smectite when DDI water is added to make a clay poultice. Therefore, the I–S in the antibacterial clay may both buffer the fluid to stabilize reduced iron and act as a potential reservoir. The cation exchange capacity of the clay minerals coupled with pyrite dissolution could explain

the elevated cation levels measured in the leachates of the Blue samples. The average CEC measurements of the bulk minerals (Fig. 7) indicate μM levels of cations can be exchanged by the clay mineral interlayer spaces. Considering the composition of the mineral leachates, Ca^{2+} and Fe^{2+} are most likely to participate in the exchange process over trivalent cations (Fe^{3+} and Al^{3+}). Since Ca^{2+} is a preferred cation in the smectite interlayer (Moore and Reynolds 1997), it could displace Fe^{2+} from exchange sites.

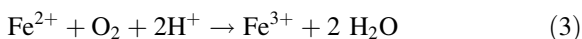
As an example, consider the water chemistry associated with the White clay from OMT. This clay, in suspension, has some antibacterial effect (Fig. 3a,b), but the aqueous leachate is only antibacterial at high mineral loading (500 mg/mL; data not shown). Given the CEC of this clay (Fig. 7), and the measured cation content of its leachate, we calculate that the smectite interlayer ‘reservoir’ could hold up to 750 μM Fe^{2+} at a 500 mg/mL mineral:water ratio. We tested the ability of smectite to be a reservoir for Fe^{2+} by saturating a standard smectite (SWy-1; Wyoming bentonite from the Clay Minerals Repository, Purdue Univ.) with Fe^{2+} . Antibacterial susceptibility testing with the Fe^{2+} -saturated smectite also showed no bacterial colonies surviving. This test confirms that smectite can be a reservoir of Fe^{2+} that is antibacterial when released by cation exchange.

Iron sulfides and reactive oxygen species (ROS)

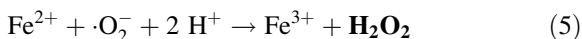
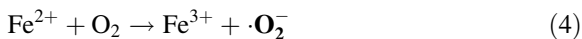
The dissolution of pyrite, under circum-neutral to alkaline pH conditions, is a function of the dissolved molecular O_2 content according to Reaction 1 (below). However, Fe^{3+} is the major oxidant in acidic (pH<4) conditions (Reaction 2) (Moses and Herman 1991; Evangelou 1995). Pyrite oxidation rates by Fe^{3+} , at pH < 4, are therefore limited by oxidation rates of ferrous iron (Fe^{2+}) in solution by dissolved O_2 (Garrels and Thompson 1960; Singer and Stumm 1970), with a rate constant of approximately 10^{-3} mol/L min (Reaction 3) (Morgan and Lahav 2007; Stumm and Morgan 1996). Cohn et al. (2006) showed that pyrite spontaneously generates ROS through a series of intermediate reactions (Reactions 4–6). Superoxide anions ($\cdot\text{O}_2^-$) and hydrogen peroxide (H_2O_2) are, respectively, produced via the Haber–Weiss reactions (Reactions 4, 5) and ultimately form hydroxyl radicals ($\cdot\text{OH}$) via the Fenton reaction (Reaction 6) (Rimstidt and Vaughan 2003;

Cohn et al. 2006; Schoonen et al. 2010). Pyrite, being a semi-conductor, has the ability to exchange 2 electrons (Schoonen et al. 2010) and directly forms hydrogen peroxide. Pyrite oxidation, known to cause nucleic acid degradation by $\cdot\text{OH}$ radicals, rapidly reacts with biomolecules and impedes certain cellular functions (Cadet et al. 1999; Cohn et al. 2006). Exploring these reactions involving ROS might explain the observed bactericidal activity caused by OMT Blue samples.

Stable reactions:



Intermediate reactions:



Toxicity of mineral leachates

All metal concentrations in mineral leachates when reacted with bacteria in a 1:1 ratio are below published MBCs for *E. coli* (Table 2, Nies 1999, 2000, 2003; Harrison et al. 2005), which were measured at circumneutral pH. However, not only the metal concentration, but its speciation, which is a function of pH and Eh, is important to consider as this determines the chemical reactions that may affect bacterial cell viability. Calcium is very high in the OMT mineral leachates because of the high Ca primary feldspars and their alteration products. It is not considered a toxic element (Borrok et al. 2004). Due to the high concentrations of Fe and Al in the antibacterial clay leachates, we determined their MIC and MBCs at the pH and Eh of the aqueous leachates.

Antibacterial susceptibility testing and analysis of the leachate chemistry allows the estimation of MIC and MBC values for mixtures of these potentially toxic elements. The MIC and MBC values for mixtures of Al^{3+} , Fe^{2+} , and Fe^{3+} were calculated from the Blue 2 leachate elemental analysis, ferrous/ferric iron assay, and antibacterial susceptibility testing of leachates reacted in a 1:1 ratio (Cells in LB:leachate). Calculation of the ferrous/ferric iron MIC's and MBC's values was achieved using the $\text{Fe}^{2+}:\text{Fe}^{3+}$ ratio of the

Blue 2 sample (1.02) and ICP-MS data. The MIC's values for Al^{3+} , Fe^{2+} , and Fe^{3+} are 550, 753, and 724 μM , respectively, while the MBC values for Al^{3+} , Fe^{2+} , and Fe^{3+} are 1.2, 1.8, and 1.7 mM, respectively. The dissolution of pyrite in the OMT Blue samples explains the low pH and presence of both Fe^{2+} and Fe^{3+} in the aqueous leachates. It is not possible to determine how much dissolution of the clay components has occurred in 24 h of mineral leaching; however, dissolution of the nano-scale amorphous iron sulfides coupled with desorption of Fe^{2+} from smectite interlayers likely provides most of the aqueous Fe^{2+} . Notably, the leachates contain complexation mixtures (Table 2) that may work synergistically to produce the observed bactericidal activity at lower MIC and MBC concentrations than reported in previous studies (Nies 1999; Harrison et al. 2005). The majority of studies on bacterial metal toxicity utilize buffered nutrient broth near circumneutral pH, which likely alters the redox state and causes pH-sensitive metals to precipitate (Nies 1999; Harrison et al. 2005). Clearly, exposure of bacterial cells to metal concentrations exceeding microbial demand requires rapid homeostatic responses to prevent cell death.

Bacterial cells exposed to elevated metal concentrations rapidly express various uptake systems that attempt to moderate toxic metal entry into the cytoplasm (Nies 1999). Metal resistance systems rely primarily on efflux mechanisms to actively remove intracellular metals (Mullen et al. 1989). More energetically demanding methods of metal resistance include complexation onto thiol-containing molecules and alteration of redox to allow toxin efflux (Nies 1999). Bacterial cells exposed to Fe^{2+} , Fe^{3+} , and Al^{3+} in the presence of ROS are subject to lipid peroxidation and oxidation of membrane proteins (Halliwell and Chirico 1993; Gutteridge 1995; Tang et al. 2000; Cabisco et al. 2000). Lipid peroxidation by Fe^{2+} has also been shown to increase in the presence of other divalent and trivalent cations (Al^{3+} , Fe^{3+} , Pb^{2+}) by potentially altering lipid membrane structure to promote peroxidation (Gutteridge 1995; Aruoma et al. 1989). The chemical mechanism that produces the observed antimicrobial action is still under investigation, but this comparative study of the mineralogical and chemical constraints on the process leads us to focus on the chemistry of iron in pathogenic bacteria and the chronic wound environment.

Medicinal applications of natural minerals

Finally, we can use the information gathered in this study to propose a medicinal application of natural clays, or the chemical process(es) they promote, toward wound healing. Chronic non-healing wounds typically exhibit more alkaline pH levels than acute wounds (Leveen et al. 1973; Gethin et al. 2007). The surface pH of healthy skin cells is slightly acidic (pH 4–6.3) which lowers potential bacterial colonization levels (Lambers et al. 2006; Schneider et al. 2007). High bacterial populations in chronic wounds shift the environment to more alkaline pH (7.3–8.9) and only heal upon transition to more acidic pH (5–6) conditions (Leveen et al. 1973; Gethin et al. 2007; Schneider et al. 2007). This increased alkalinity decreases the release of oxygen from hemoglobin (Gethin 2007; Leveen et al. 1973) causing a more reduced environment with Eh values ranging from -140 to -400 mV (Bullen et al. 2006). In healthy muscle tissue, Eh values are ≥ 300 mV, which helps keep iron oxidized (Fe^{3+}) and bound in transferrin (Bullen et al. 2006). When wound Eh falls below -140 mV (at pH 7.3–8.9), Fe^{3+} is reduced to Fe^{2+} and no longer bound by transferrin. This makes Fe^{2+} available for bacterial metabolic activities (Bullen et al. 2006).

Conventional thinking is that Fe^{3+} within chronic wounds is a limiting nutrient for bacterial growth due to its low solubility (10^{-18} M) at physiological pH (~ 7) (Ratledge and Dover 2000). Iron in mammals is transferred in the blood stream by the proteins transferrin and hemoglobin while cellular storage occurs within ferritin. Pathogenic bacteria access this Fe through direct contact and siderophore production, which ultimately leads to host cell breakdown (Ratledge and Dover 2000). Use of iron-chelating compounds prevents pathogenic bacterial use of intracellular Fe and has been employed as a treatment option (Taylor et al. 2005). In contrast to the conventional medical strategy of limiting bacterial iron supplies, recent evidence suggests that excess iron levels can perturb biofilm formation by repressing pathogen virulence factor formation (Harrison et al. 2005; Musk et al. 2005). Therefore, careful applications of natural minerals generating excess soluble iron may similarly limit pathogenic bacterial growth and/or biofilm development. Furthermore, due to the highly absorptive surfaces of clay minerals (especially smectite), these clays may aid in wound debridement

including removal of abnormal collagen tissue and toxic bacterial products (e.g. NH_4^+).

In many clinical trials, chronic wound acidification has been advocated as a treatment option (Leveen et al. 1973; Gethin 2007; Kaufman et al. 1985) and successfully eliminated many problems associated with alkaline wound environments (Liu et al. 2002; Gethin 2007; Schneider et al. 2007). Manuka honey and acidified nitrite are examples of acidifying agents (pH 3–4.5) that have been used in chronic wound care (Gethin et al. 2008; Weller et al. 2001, 2006). However, acidification with solutions (e.g., 1 % acetic acid) can only maintain an acidic environment for up to an hour, so compounds that buffer an acidic environment are needed (Leveen et al. 1973; Gethin et al. 2008). Another viable option for chronic wound healing is hyperbaric oxygen therapy, which raises the tissue oxygen levels (Leveen et al. 1973; Roth and Weiss 1994). Although both hyperbaric oxygen and acidified nitrite can produce damaging ROS and reactive nitrogen species (RNS), these therapies have been shown to promote skin cell growth (Weller et al. 2001; Alleva et al. 2005; Weller and Finnen 2006).

Similar to these accepted treatments of chronic wounds, the antibacterial OMT clays, due to their buffering capacity (Fig. 8), can stabilize an aqueous environment to $\text{pH} < 4$ with elevated Eh (>630 mV) relative to chronic wound environments (Fig. 9). The OMT clays are acidic (2.5–3.1) and can potentially maintain lower pH for many hours due to their buffering capacity and continued release of H^+ during pyrite oxidation. In mammalian cells, macrophages and neutrophils utilize a burst of ROS to fight invading pathogens (Fang 2004). However, the alkaline pH levels in chronic wounds lead to hypoxic conditions making such a respiratory burst of ROS difficult (Roy et al. 2006). The application of antibacterial minerals to wounds may function in wound healing by lowering the pH of a chronic wound from alkaline conditions allowing the release of oxygen from hemoglobin while potentially generating reactive oxygen species resulting in a burst of ROS similar to those utilized by macrophages. Figure 9 shows the stability fields for the OMT clays relative to that of chronic wounds. Antibacterial samples from the OMT deposit may shift the pH and Eh in chronic non-healing wounds to a range that favors healing while killing invading pathogens. The titration curves plotted demonstrate the ability of the antibacterial clays to buffer the Eh,

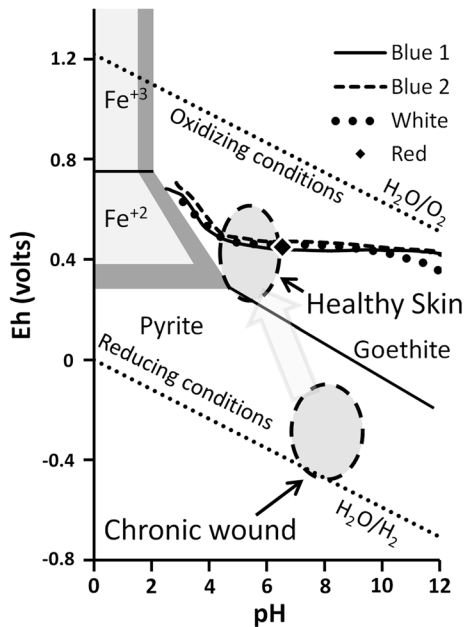


Fig. 9 Eh and pH mineral stability diagram of the Fe–S–O–H system. Light gray and dark gray iron stability regions representing 10^{-3} and 10^{-6} M concentrations are superimposed. Sulfur concentrations were kept at 10^{-3} M. Eh–pH titrations using 0.1 N NaOH and 100 mg/mL mineral suspensions of OMT samples are shown by solid and dashed lines (legend). Dashed ovals represent the Eh and pH values found in chronic non-healing wounds versus healthy skin (Leveen et al. 1973; Gethin 2007; Bullen et al. 2006)

given changes in pH, whereas the non-antibacterial sample (Red) is not an effective buffer (Fig. 8). The ability of the antibacterial clays to raise the Eh of a chronic wound and lower the pH to conditions of healthy skin is key to their healing potential.

Conclusions

Clays are a mixture of <2.0 μm minerals that have equilibrated with pore fluids in natural geologic environments. Their mineral chemistries are controlled by environmental temperature, pressure, and fluid composition. When clays are taken from natural formations and hydrated at room temperature and pressure with oxygenated DDI water, as applied to skin infections (Williams et al. 2004), the minerals re-equilibrate, potentially dissolving (by oxidation) or exchanging cations and anions. In this novel study, we show that different mineralogical assemblages within

the natural OMT clay deposit demonstrate varying antibacterial effectiveness on model gram-negative and gram-positive bacteria.

Selecting representative samples from three different alteration zones, within the OMT deposit, we conclude that samples containing pyrite and mixed-layered illite–smectite (Blue zone) are the most effective at killing the model pathogens tested (*E. coli* and *S. epidermidis*); however, samples without pyrite (White zone) also reduce these bacterial populations by 5 and 3 orders of magnitude, respectively. The mixed-layered illite–smectite plays an important role as a buffer and reservoir of cations, producing the antibacterial effect observed in clays not containing pyrite. The dominant illite layers (in illite–smectite) can protect the expandable smectite layers from dissolution, allowing adsorption of Fe^{2+} (or other transition metals) into their stabilizing acidic inter-layers. The mixed-layered illite–smectite also provides a delivery mechanism for the release of transition metals while maintaining hydration during application.

Because the hydrated Blue and White clays remained bactericidal over a 24 h period, this study focused on fluid chemical changes within this time-frame. The antibacterial effectiveness correlates with elevated concentrations of Fe^{2+} , Fe^{3+} , and Al^{3+} in the aqueous leachates. Unoxidized Blue samples appeared most antibacterial and released the highest iron levels (18 mM) in their aqueous leachates. All antibacterial clay samples contained Fe^{2+} and buffered solutions to acidic pH (2.5–3.1) and oxidizing Eh (630–706 mV) conditions. High levels of aluminum and calcium alone do not explain observed antibacterial activity because they are below published MICs for the bacteria tested. However, the high Fe^{2+} or combinations of the other soluble elements with Fe might ultimately control the antibacterial process(es).

Bioimaging of bacteria by TEM, after exposure to aqueous mineral suspensions of the Blue clay, indicated no evidence of cell lysis; however, cytoplasmic condensation and appearance of electron dense intracellular particles occurred after 8 h. These particles were determined to be Fe-oxides which likely formed from the rapid influx of Fe^{2+} , forming ROS that attack cell components and precipitate Fe^{3+} oxides. However, extracellular attack of the cells appears to occur as well, as shown by formation of electron dense regions on the cell walls suggesting adsorption or

precipitation of metals. Extracellular adsorption of Fe^{+2} , Fe^{3+} , and Al^{3+} may result in lipid and protein oxidation increasing membrane permeability and allowing the influx of toxic metals. Therefore, it may be a combination of cell wall attack and intracellular reactions that result in cell death or significant viability loss within the experimental time frames.

Clays containing minerals that buffer solutions to healthy skin pH, Eh conditions and produce soluble Fe^{2+} could be viable treatment options for chronic (non-healing) wounds infected with antibiotic-resistant bacteria. One goal of this work involved characterizing mineralogical variables related to antibacterial effectiveness and identifying new clay deposits which exhibit consistent, antibacterial capacities. Such natural deposits may provide cost-effective topical antibacterial treatments or lead to discovery of new antibacterial mechanisms that may ultimately benefit the health care industry and developing nations by providing a low cost topical antibacterial agent that arises from the hydrothermal alteration of volcanic rock.

Acknowledgments The authors are grateful for the use of the United States Geological Survey (Boulder CO), X-ray Diffraction Lab. Various laboratories at Arizona State University supported this work, and we thank David Lowry and Robert Roberson in the School of Life Sciences (SOLS) Bioimaging Facility—Electron microscopy division; Stanley Williams for observations in the field; Sandra Londoño Arias for assistance with the TEM; Thomas Groy for XRD facilities at ASU; Everett Shock for use of his biogeochemistry lab; Steve Romaneillo for ICP-MS analyses in the W.M. Keck Foundation Laboratory for Environmental Biogeochemistry; Rajeev Misra (SOLS) and Amisha Poret-Peterson in the Astrobiology Inst. for help with microbiology techniques; Karl Weiss and Jiangtao Zhu in the LeRoy Eyring Center for Solid State Science for help with the STEM-EELS imaging. This research was funded by Grant (EAR-1123931) from the National Science foundation, the Clay Minerals Society, and the Geological Society of America.

References

- Alleva, R., Nasole, E., Di Donato, F., Borghi, B., Neuzil, J., & Tomasetti, M. (2005). α -Lipoic acid supplementation inhibits oxidative damage accelerating chronic wound healing in patients undergoing hyperbaric oxygen therapy. *Biochemical and Biophysical Research Communications*, *300*, 404–410.
- Anastácio, A. S., Harris, B., Yoo, H., Fabris, J. D., & Stucki, J. W. (2008). Limitations of the ferrozine method for quantitative assay of mineral systems for ferrous and total iron. *Geochimica et Cosmochimica Acta*, *72*, 5001–5008.
- Aran, D., Maul, A., & Masfaraud, J. (2008). A spectrophotometric measurement of soil cation exchange capacity based on cobaltihexamine chloride absorbance. *C.R. Geoscience*, *340*, 865–871.
- Aruoma, O. I., Halliwell, B., Laughton, M. J., Quinlan, G. J., & Gutteridge, J. M. C. (1989). The mechanism of interaction of lipid peroxidation. Evidence against a requirement for an iron(II)-iron(III) complex. *Biochemistry Journal*, *258*, 617–620.
- Bacon, C. R. (2008). Geologic map of Mount Mazama and Crater Lake caldera, Oregon. *U.S Geological Survey Scientific Investigations Map*, 2832, 1–47.
- Bhowal, S., & Chakraborty, R. (2011). Five novel acid-tolerant oligotrophic thiosulfate-metabolizing chemolithotrophic acid mine drainage strains affiliated with the genus *Burkholderia* of *Betaproteobacteria* and identification of two novel soxB gene homologues. *Research in Microbiology*, *162*, 436–445.
- Borrok, D., Fein, J. B., Tischler, M., O'Loughlin, E., Meyer, H., Liss, M., et al. (2004). The effect of acidic solutions and growth conditions on the adsorptive properties of bacterial surfaces. *Chemical Geology*, *209*, 107–119.
- Brunet de Courrou L. (2002). *Study Group Report on Buruli ulcer treatment with clay*, 5th WHO Advisory Group Meeting on Buruli Ulcer, Geneva, Switzerland.
- Bullen, J. J., Rogers, H. J., Spalding, P. B., & Ward, C. G. (2006). Natural resistance, iron and infection: A challenge for clinical medicine. *Journal of Medical Microbiology*, *55*, 251–258.
- Cabiscol, E., Tamarit, J., & Ros, J. (2000). Oxidative stress in bacteria and protein damage by reactive oxygen species. *International Microbiology*, *3*, 3–8.
- Cadet, J., Delatour, T., Douki, T., Gasparutto, D., Pouget, J. P., Ravanat, J. L., et al. (1999). Hydroxyl radicals and DNA base damage. *Mutation Research*, *424*, 9–21.
- Carretaro, M. I. (2002). Clay minerals and their beneficial effects upon human health. A review. *Applied Clay Science*, *21*, 155–163.
- Church, C. D., Wilkin, R. T., Alpers, C. N., Rye, R. O., & McCleskey, R. B. (2007). Microbial sulfate reduction and metal attenuation in pH 4 acidic mine water. *Geochemical Transactions*, *8*, 1–14.
- Cohn, C. A., Laffers, R., Simon, S. R., O'Riordan, T., Schoonen, & M. A. A. (2006). Role of pyrite in formation of hydroxyl radicals in coal: Possible implications for human health. *Particle and Fibre Toxic*, *3*(article 16), 1–10.
- Cunningham, T. B., Koehl, J. L., Summers, J. S., & Haydel, S. E. (2010). pH-dependent metal ion toxicity influences of the antibacterial activity of two natural mineral mixtures. *PLoS-ONE*, *5*, e9456.
- Derkowski, A., & Bristow, T. F. (2012). On the problems of total specific surface area and cation exchange capacity measurements in organic-rich sedimentary rocks. *Clays and Clay Minerals*, *60*, 348–362.
- Dick, J. M. (2008). Calculation of the relative metastabilities of proteins using the CHNOSZ software package. *Geochemical Transactions*, *9*(10), 1–17.
- Dold, B. (2005). *Basic concepts in environmental geochemistry of sulfide mine-waste*, Del 22 de Agosto al 2 de Sept. XXIV Curso Latinoamericano de Metalogenia UNESCO-SEG.
- Eberl, D. D. (2007). User's guide to rockjock: A program for determining quantitative mineralogy from powder X-ray

- diffraction data. *U.S. Geological Survey*, Open-file report 03–78.
- Evangelou, V. P. (1995). *Pyrite oxidation and its control*. New York: CRC Press.
- Fang, F. C. (2004). Antimicrobial reactive oxygen and nitrogen species: Concepts and controversies. *Nature Reviews Microbiology*, 2, 820–832.
- Ferrell, R. E. (2008). Medicinal clay and spiritual healing. *Clays and Clay Minerals*, 56, 751–760.
- Ferrero, T. (1992). Geologic mapping and sampling project, Foster Creek sulfur deposit. *Company Report, Ferrero Geologic*, 340 Avery St. Ashland Oregon, 97520.
- Galan, E., Carretero, M. I., & Fernandez-Caliani, J. C. (1999). Effects of acid mine drainage on clay minerals suspended in the Tinto River (Río Tinto, Spain). An experimental approach. *Clay Minerals*, 34, 99–108.
- Garrels, R. M., & Thompson, M. E. (1960). Oxidation of pyrite by iron sulfate solutions. *American Journal of Science*, 258-A, 57–67.
- Gethin, G. T. (2007). The significance of surface pH in chronic wounds. *Wounds UK*, 3, 52–56.
- Gethin, G. T., Cowman, S., & Conroy, R. M. (2008). The impact of Manuka honey dressings on the surface pH of chronic wounds. *International Wound Journal*, 5, 185–194.
- Götz, F. (2002). *Staphylococcus* and biofilms. *Molecular Microbiology*, 43, 1367–1378.
- Gutteridge, J. M. C. (1995). Lipid peroxidation and antioxidants as biomarkers of tissue damage. *Clinical Chemistry*, 41, 1819–1828.
- Halliwel, B., & Chirico, S. (1993). Lipid peroxidation: Its mechanism, measurement, and significance. *American Journal of Clinical Nutrition*, 57, 715s–725s.
- Hanaichi, T., Sato, T., Iwamoto, T., Malavasi-Yamashiro, J., Hoshing, M., & Mizuno, N. (1986). A stable lead by modification of Sato's method. *Journal of Electron Microscopy*, 35, 304–306.
- Harrison, J. J., Turner, R. J., & Ceri, H. (2005). High-throughput metal susceptibility testing of microbial biofilms. *BMC Microbiology*, 5, 1–11.
- Hutchinson, I. P. G., & Ellison, R. D. (1992). *Mine waste management*. Lewis publishers, INC. 121 S. Main St. Chelsea, Michigan.
- Isakow, W., & Micek, S. T. (2006). Methicillin-resistant *staphylococcus aureus* pneumonia-current and future therapeutic options. *US Respiratory Disease* 62–64.
- Kaufman, T., Eichenlaub, E. H., Angel, M. F., Levin, M., & Futrell, J. W. (1985). Topical acidification promotes healing of experimental deep partial thickness skin burns: A randomized double-blind preliminary study. *Burns*, 12, 84–90.
- Komadel, P., & Stucki, J. W. (1988). Quantitative assay of minerals for Fe²⁺ and Fe³⁺ using 1,10-phenanthroline: III. A rapid photochemical method. *Clays and Clay Minerals*, 36, 379–381.
- Lambers, H., Piessens, S., Bloem, A., Pronk, H., & Finkel, P. (2006). Natural skin surface pH is on average below 5, which is beneficial for its resident flora. *International Journal of Cosmetic Science*, 28, 359–370.
- Lawrence, J. R., Swerhone, G. D. W., Leppard, G. G., Araki, T., Zhang, X., West, M. M., et al. (2003). Scanning transmission X-ray, laser scanning, and transmission electron microscopy mapping of the exopolymeric matrix of microbial biofilms. *Applied and Environment Microbiology*, 69, 5543–5554.
- Lemire, J. A., Harrison, J. J., & Turner, R. J. (2013). Antimicrobial activity of metals: mechanisms, molecular targets and applications. *Nature Reviews*, 11, 371–384.
- Leveen, H. H., Falk, G., Borek, B., Diaz, C., Lynfield, Y., Wynkoop, B. J., et al. (1973). Chemical acidification of wounds: An adjuvant to healing and the unfavorable action of alkalinity and ammonia. *Annals of Surgery*, 178, 745–753.
- Liss, S. N., Droppo, I. G., Flannigan, D. T., & Leppard, G. G. (1996). Floc architecture in wastewater and natural riverine systems. *Environmental Science and Technology*, 30, 680–686.
- Liu, Y., Kalen, A., Risto, O., & Whalstrom, O. (2002). Fibroblast proliferation due to exposure to a platelet concentrate in vitro is pH dependent. *Wound Repair and Regeneration*, 10, 336–340.
- Meunier, A. (2005). *Clays*. Berlin, Heidelberg, New York: Springer.
- Moore, D. M., & Reynolds, R. C. (1997). *X-ray diffraction and the identification and analysis of clay minerals* (2nd ed.). New York: Oxford University Press.
- Morgan, B., & Lahav, O. (2007). The effect of pH on the kinetics of spontaneous Fe(II) oxidation by O₂ in aqueous solution—basic principles and a simple heuristic description. *Chemosphere*, 68, 2080–2084.
- Moses, C. O., & Herman, J. S. (1991). Pyrite oxidation at circumneutral pH. *Geochimica et Cosmochimica Acta*, 55, 471–482.
- Mullen, M. D., Wolf, D. C., Ferris, F., Beveridge, T. J., Fleming, C. A., & Bailey, G. W. (1989). Bacterial sorption of heavy metals. *Applied Environmental Microbiology*, 55, 3143–3149.
- Murad, E., & Rojik, P. (2004). *Jarosite, schwertmannite, goethite, ferrihydrite and lepidocrocite: The legacy of coal and sulfide ore mining*. Super Soil 2004: 3rd Australian New Zealand Soils Conference, Dec 2004, University of Sydney, Australia.
- Murad, E., & Rojik, P. (2005). Iron mineralogy of mine drainage precipitates as environmental indicators: Review of the current concepts and a case study from the Sokolov Basin, Czech Republic. *Clay Minerals*, 40, 427–440.
- Musk, D. J., Banko, D. A., & Hergenrother, P. J. (2005). Iron salts perturb biofilm formation and disrupt existing biofilms of *Pseudomonas aeruginosa*. *Chemistry and Biology*, 12, 789–796.
- Nies, D. H. (1999). Microbial heavy-metal resistance. *Applied Microbiology and Biotechnology*, 51, 730–750.
- Nies, D. H. (2000). Heavy metal-resistant bacteria as extremophiles: Molecular physiology and biotechnological use of *Ralstonia* sp. CH34. *Extremophiles*, 4, 77–82.
- Nies, D. H. (2003). Efflux-mediated heavy metal resistance in prokaryotes. *FEMS Microbiology Reviews*, 27, 313–339.
- Ratledge, C., & Dover, L. G. (2000). Iron metabolism in pathogenic bacteria. *Annual Review of Microbiology*, 54, 881–941.
- Reynolds, R. C. (1985). NEWMOD© a computer program for the calculation of one-dimensional diffraction patterns of mixed layered clay minerals. In R. C. Reynolds, 8 Brook Rd, Hanover, New Hampshire, 03755, USA.

- Rimstidt, J. D., & Vaughan, D. J. (2003). Pyrite oxidation: A state of the art assessment of the reaction mechanism. *Geochimica et Cosmochimica Acta*, 67, 873–880.
- Roth, R. N., & Weiss, L. D. (1994). Hyperbaric oxygen and wound healing. *Clinics in Dermatology*, 12, 141–156.
- Roy, S., Khanna, S., Nallu, K., Hunt, T. K., & Sen, C. K. (2006). Dermal wound healing is subject to redox control. *Molecular Therapy*, 1, 211–220.
- Schneider, L. A., Korber, A., Grabbe, S., & Dissemmond, J. (2007). Influence of pH on wound-healing: A new perspective for wound therapy? *Archives of Dermatological Research*, 298, 413–420.
- Schoonen, M. A. A., Harrington, A. D., Laffers, R., & Strongin, D. R. (2010). Role of hydrogen peroxide and hydroxyl radical in pyrite oxidation by molecular oxygen. *Geochimica et Cosmochimica Acta*, 74, 4971–4987.
- Shaw, S. A., & Hendry, M. J. (2009). Geochemical and mineralogical impacts of H₂SO₄ on clays between pH 5.0 and 3.0. *Applied Geochemistry*, 24, 333–345.
- Silhavy, T. J., Kahne, D., & Walker, S. (2010). The bacterial cell envelope. *Cold Spring Harbor Perspectives in Biology*, 2, a000414.
- Sillitoe, R. H., Hedenquist, J. W. (2003). Linkages between volcanotectonic settings, ore-fluid compositions, and epithermal precious metal deposits, *Society of Economic Geologists, Special Publication*, 10.
- Singer, P. C., & Stumm, W. (1970). Acid mine drainage the rate determining step. *University of Toronto Study, Geological Survey*, 44, 83–93.
- Smith, J. L. (2004). The physiological role of ferritin like compounds in bacteria. *Clinical Reviews in Microbiology*, 30, 173–185.
- Spurr, A. R. (1969). A low-viscosity epoxy resin embedding medium for electron microscopy. *Journal of Ultrastructural Research*, 26, 31–43.
- Stumm, W., & Morgan, J. J. (1996). *Aquatic chemistry. Chemical equilibria and rate constants in natural waters* (3rd ed.). New York: Wiley.
- Tang, L., Zhang, Y., Qian, Z., & Shen, X. (2000). The mechanism of Fe²⁺-initiated lipid peroxidation in liposomes: The dual function of ferrous ions, the roles of the pre-existing lipid peroxides and the lipid peroxy radical. *Biochemical Society Journal*, 352, 27–36.
- Taylor, J. E., Laity, P. R., Hicks, J., Wong, S. S., Norris, K., Khunkamchoo, P., et al. (2005). Extent of iron pick-up in deferoxamine-coupled polyurethane materials for therapy of chronic wounds. *Biomaterials*, 26, 6024–6033.
- Totsche, O., Fyson, A., Kalin, M., & Steinberg, C. E. W. (2006). Titration curves-A useful instrument for assessing the buffer systems of acidic mining waters. *Environmental Science and Pollution Research*, 13, 215–224.
- Urrutia, M. M., & Beveridge, T. J. (1995). Formation of short-range ordered aluminosilicates in the presence of a bacterial surface (*Bacillus subtilis*) and organic ligands. *Geoderma*, 65, 149–165.
- Valverde, A., Delvasto, P., Peix, A., Velazquez, E., Santa-Regina, I., Ballester, A., et al. (2006). *Burkholderia ferrariae* sp. Nov., isolated from an iron ore in Brazil. *International Journal of Systematic and Evolutionary Microbiology*, 56, 2421–2425.
- Weller, R., & Finnen, M. J. (2006). The effects of topical treatment with acidified nitrite on wound healing in normal and diabetic mice. *Nitric Oxide*, 15, 395–399.
- Weller, R., Price, R. J., Ormerod, A. D., Benjamin, N., & Leifert, C. (2001). Antimicrobial effect of acidified nitrite on dermatophyte fungi. *Candida* and bacterial skin pathogens. *Journal of Applied Microbiology*, 90, 648–652.
- Williams, R. J. P. (1999). What is wrong with aluminium? The J.D. Birchall memorial lecture. *Journal of Inorganic Biochemistry*, 76, 81–88.
- Williams, L. B., & Haydel, S. E. (2010). Evaluation of the medicinal use of clay minerals as antibacterial agents. *International Geology Review*, 52(7–8), 745–770.
- Williams, L. B., Haydel, S. E., Giese, R. F., & Eberl, D. D. (2008). Chemical and mineralogical characteristics of French green clays used for healing. *Clays and Clay Minerals*, 56, 437–452.
- Williams, L. B., Holland, M., Eberl, D. D., Brunet, T., & Brunet de Courssou, L. (2004). Killer clays! Natural antibacterial clay minerals. *Mineralogical Society Bulletin*, 139, 3–8.
- Williams, L. B., Metge, D. W., Eberl, D. D., Harvey, R. W., Turner, A. G., Prapaipong, P., et al. (2011). What makes a natural clay antibacterial? *Environmental Science and Technology*, 45, 3768–3773.
- Wilson, E., Henry, D. A., & Smith, J. A. (1990). Disk elution method for MICs and MBCs. *Antimicrobial Agents and Chemotherapy*, 34, 2128–2132.
- Yariv, S. (1992). The effect of tetrahedral substitution of Si by Al on the surface acidity of the oxygen plane of clay minerals. *International Reviews in Physical Chemistry*, 11, 345–375.
- Yariv, S., & Cross, H. (2002). *Organo-clay complexes and interactions* (pp. 1–38). New York: Marcel Dekker, Inc.